Journal of Quantitative Spectroscopy & Radiative Transfer 135 (2014) 81–89

Contents lists available at ScienceDirect

Journal of Quantitative Spectroscopy & Radiative Transfer

journal homepage: www.elsevier.com/locate/jqsrt

Study of magnetic polaritons in deep gratings for thermal emission control

Bo Zhao, Zhuomin M. Zhang *

George W. Woodruff School of Mechanical Engineering, Georgia Institute of Technology, Atlanta, GA 30332, USA

ARTICLE INFO

Article history:
Received 2 August 2013
Received in revised form
16 November 2013
Accepted 21 November 2013
Available online 28 November 2013

Keywords:
Cutoff wavelength
Deep gratings
LC-circuit model
Magnetic polaritons
Spectral-selective thermal emitters

ABSTRACT

Recently, it has been shown that convex cavities or 2D grating structures can enhance thermal emission for energy conversion systems. The mechanisms, however, cannot be well explained by either the conventional cavity resonance modes or surface plasmon polaritons. The present study elucidates the fundamental mechanism by considering the excitation of magnetic polaritons (MPs) in deep gratings. Rigorous coupled-wave analysis (RCWA) is employed to calculate the radiative properties by solving Maxwell's equations numerically. The LC-circuit model is employed to predict the resonance conditions. The current and field distributions further confirm the excitation of magnetic resonances. It is shown that MPs and cavity modes agree with each other when the kinetic inductance is negligibly small. However, when the kinetic inductance is sufficiently large, the maximum resonance wavelength can be more than twice that predicted by the cavity mode. Furthermore, different materials are considered and the frequency range is extended from the near-infrared to the microwave region to illustrate the scalability of the MPs. This study clarifies one of the underlying mechanisms of optical resonance in deep gratings and will benefit the design of wavelength-selective thermal emitters.

1. Introduction

Generated by the thermal motion of charged particles in matter, thermal radiation is usually incoherent. Researchers have put significant effort towards controlling thermal radiation for applications such as solar cells [1–4] and thermophotovoltaic (TPV) systems [5–9], in which it is desired to have a receiver (or emitter) that can absorb (or emanate) radiation only in certain wavelength regions. One-, two-, or three-dimensional (1D, 2D, or 3D) micro/nanoperiodic structures of wide profile diversity and dimensionality can enable tailoring the radiative properties for developing spectral selective absorbers and emitters [10]. As a matter of fact, 1D and 2D gratings have been extensively investigated both theoretically and experimentally.

Hesketh et al. [11,12] experimentally demonstrated the resonance in the emission spectra with 1D doped-Si deep gratings, and explained them with an acoustic analog of the organ pipe mode. Later, Maruyama et al. [13] used the cavity resonance modes to explain the resonance conditions in 2D-microcavity gratings. Sai et al. [6] and Kusunoki et al. [14] also experimentally demonstrated resonances in similar structures as cavity modes. Though the cavity resonance theory has successfully explained the resonances in the certainty periodic structures [15], it cannot predict the maximum (or cutoff) resonance wavelength in a grating with narrow slits or trenches. As an example, the resonance wavelength can be about ten times the grating depth (or height) [16] while the cavity resonance formulation yields a maximum resonance wavelength four times the grating depth. Finite inductance [17,18], coupled surface plasmon polaritons (SPPs) [19,20], and trapped modes theory have been used to explain the mechanisms of resonances and the increase of the cutoff wavelength in gratings [21], grating/thin-film structures [22],

* Corresponding author. Tel.: +1 404 385 4225.
E-mail address: zhuomin.zhang@me.gatech.edu (Z.M. Zhang).

0022-4073/$ - see front matter © 2013 Elsevier Ltd. All rights reserved.
http://dx.doi.org/10.1016/j.jqsrt.2013.11.016

holes [17], and slits [18]. Mattiucci et al. [16] evaluated the impedance of the grating using coupled SPP modes and successfully predicted the emittance of grating structures with the metamaterial effective media approach. However, the resonance peaks could not be obtained explicitly. Pardo et al. [23] explained the funneling of light into narrow grooves etched on a metal surface as a result of magnetoelectric interference, but did not quantify the resonance condition. To guide the engineering design of nanostructures [24], it is desirable to develop simple models to predict resonance wavelength for certain kind of structures.

The theory of magnetic polaritons (MPs) has successfully been used to predict the resonances in metallic grating/thin-film structures [9,25] and narrow slit arrays [26]. Wang and Zhang [27] also used the excitation of MPs to explain the phonon-mediated resonances in SiC deep gratings. In addition, MP resonance has been used to explain the responses in the structures mentioned in [16,23]. Since the resonance in deep gratings shows different geometry dependence in different wavelength ranges, it is worthwhile to explore the possibility of using MPs to explain the anomalous maximum wavelength in deep gratings for various materials and spectral regions. In this paper, the inductor–capacitor (LC) circuit model [28,29] is used to predict the fundamental MP resonance mode in deep gratings. The results are compared with rigorous-coupled wave analysis (RCWA). The electric field and current–density distributions at the resonance condition are used to elucidate the magnetic resonance or the diamagnetism effect. Silver (Ag), heavily doped semiconductor (Si), and tungsten are considered. The resonance wavelengths are extended from the near-infrared to the microwave region by scaling the geometric dimensions of the gratings along with the wavelength.

2. Theoretical analysis

2.1. Classical cavity resonance model

Fig. 1 illustrates the 1D metallic grating structure considered in this paper. The grating is described by a period Λ, ridge width w, height (or depth) h, and trench width b. The metal filling ratio in the grating region is defined as $f=w/\Lambda$. The region below the grating is made of the same material and thick enough to be treated opaque. Consider radiation incident from air (medium above the grating) to the grating. Due to the high reflectivity of the metallic material, the reflectivity of the grating is generally high except when resonance occurs that can cause a sudden reduction of the reflectance (i.e., increase of the absorptance or emittance). The cavity resonance model has often been used to explain the emittance peaks for 2D grating or cavity structures [6,13,14]:

$$\lambda_{lmn}=\frac{2}{\sqrt{(l/L_x)^2+(m/L_y)^2+((n+\frac{1}{2})/L_z)^2}} \tag{1}$$

where l, m, and n are integers (0, 1, 2, …), and L_x, L_y, and L_z define the cavity dimensions. For a 1D grating, L_y is infinitely long such that only L_x and L_z (which are referred as b and h in Fig. 1) can affect the resonance wavelengths. The maximum value of λ_{lmn} is called the cutoff wavelength and can be determined by setting $l=n=0$ in Eq. (1), resulting in a resonance wavelength (λ_R) that is four times the grating height ($4h$). However, this value may be much smaller than the resonance wavelength in a deep grating with a high aspect ratio (h/d), as shown in the example below.

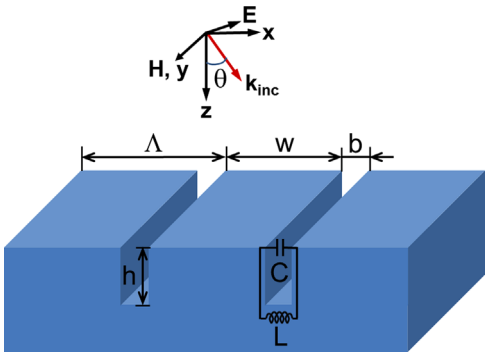

Fig. 1. Schematic of the 1D metallic grating with a period Λ, height or depth h, ridge width w, and trench width b. The equivalent LC circuit model is also shown with the capacitance C and inductance L. Only TM wave is considered so that **H** is always parallel to the y-axis. The wavevector $\mathbf{k}_{inc}$ of the incident plane wave is in the x–z plane at an angle θ with respect to the z-axis.

Fig. 2(a) shows the normal emittance spectrum of transverse magnetic (TM) waves for a Ag grating with $\Lambda=400$ nm, $h=200$ nm, and $b=5$ nm. The calculation is based on RCWA that solves the Maxwell equations numerically to determine the spectral reflectance and then calculate the emittance as one minus the reflectance [7,25]. The optical properties of Ag are obtained using the Drude model with the following parameters [30,31]: plasma frequency $\omega_p=1.39\times10^{16}$ rad/s, scattering rate $\gamma=2.7\times10^{13}$ rad/s, and a high-frequency constant $\varepsilon_\infty=3.4$. The emittance spectrum is characterized by a peak as high as 0.85 at the wavelength of 2.74 μm. The emittance enhancement is remarkable since the emittance is less than 0.005 for a smooth Ag surface at this wavelength. Note that λ_R for this mode is nearly 14 times the grating height. This resonance cannot be explained by SPP or Wood's anomaly since both of which would occur at much short wavelengths on the order of period [7,30]. Furthermore, the high emittance is almost omnidirectional as seen from the contour plot displayed in Fig. 2(b), which shows the directional spectral emittance in terms of the wavenumber and parallel wavevector $k_x=k_{inc}\sin\theta$. Emittance values at $k_x=0$ (i.e., along the ordinate) correspond to normal incidence with an emittance peak located at 3650 cm^{-1}. A quantitative explanation is given below using the MP model that takes account of the geometry and material's properties.

2.2. Magnetic polaritons and the LC-circuit model

Magnetic polaritons refer to the strong coupling of the magnetic resonance inside a micro/nanostructure with the external electromagnetic waves. Under a time-varying magnetic field parallel to the y-direction, an oscillating current is produced around the grooves in the x–z plane, and this induced current generates a magnetic field (i.e., diamagnetism) according to Lenz's law. Fig. 3(a) and (b) shows the electromagnetic and current–density field

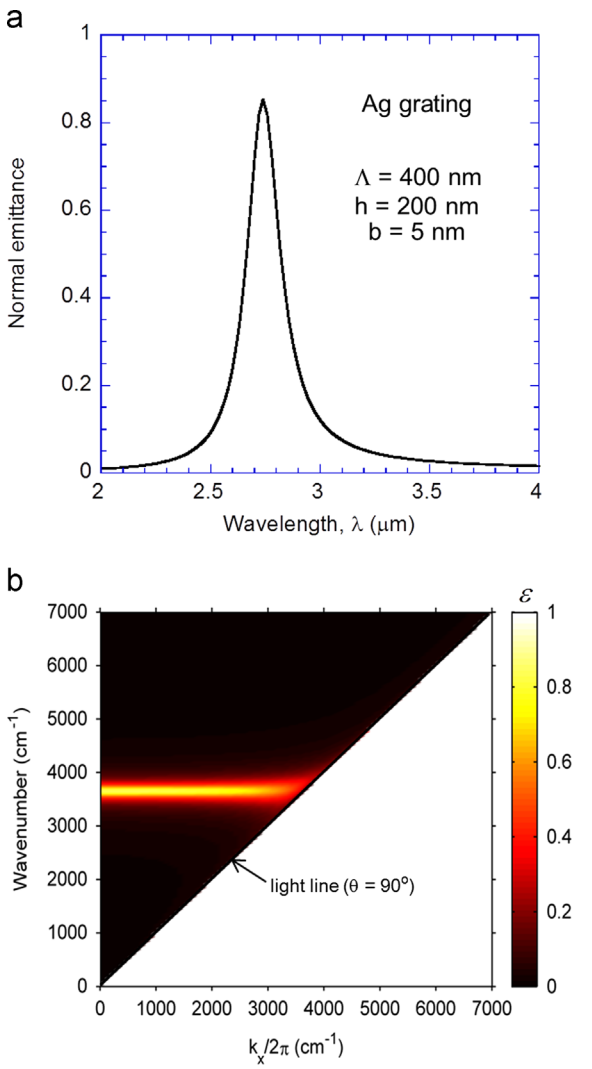

Fig. 2. Emittance for Ag deep gratings with $\Lambda=400$ nm, $h=200$ nm, and $b=5$ nm: (a) normal spectral emittance; (b) contour plot of the emittance in terms of the wavenumber and parallel component of the wavevector. The vertical line with $k_x=0$ represents normal direction and the diagonal represents grazing angle or light line.

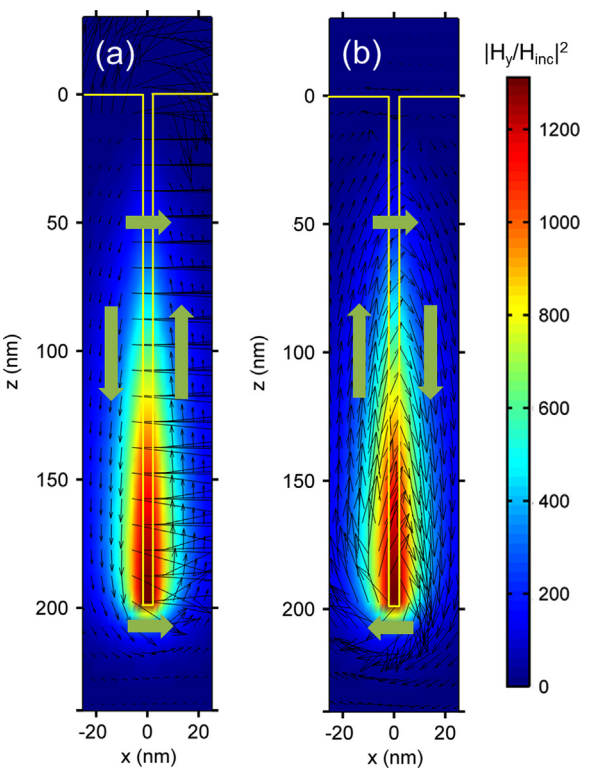

Fig. 3. (a) The electromagnetic field and (b) current–density distribution in the Ag grating with the same parameters as for Fig. 2 at $\lambda=\lambda_R=2.74$ μm. The color contour shows the relative magnitude of the y component of the magnetic field. The vectors show the direction and magnitude of the electric field in (a) and current density in (b). Note that positive z-direction is downward. (For interpretation of the references to color in this figure legend, the reader is referred to the web version of this article.)

when the resonance occurs in the aforementioned Ag grating. The x–y plane is at the interface between the grating and air; besides, $x=0$ is located at the center of a trench. The electric field and current–density vectors, denoted by the arrows, are the instantaneous values at time $t=0$, while the magnetic field, represented by the color contour, is the square of the relative amplitude. Since the instantaneous electric and current–density field vectors oscillate with time, the direction of the arrows may reverse. The big arrows show the general direction of the vectors. The electric field at the opening is greatly enhanced and decays nearly linearly towards the bottom. The current–density vectors are obtained from $\mathbf{J}=\sigma\mathbf{E}$ where σ is the complex electrical conductivity of the material at the given location [30], and they form a closed loop around the trench. The electric current consists of two parts: displacement current and conduction current. The conduction current is directly related to the real part of $\mathbf{E}$, which is the instantaneous electric field. However, the displacement current is related to the imaginary part of $\mathbf{E}$. As it turns out, the signs of the current and field differ in the Ag wall, as indicated by the big arrows. Therefore, the current forms a closed loop while the electric field does not, similar to the observations made previously for a different structure [25]. The strongest magnetic enhancement corresponding to the closed current loop is at the bottom of the trench, where the magnitude of magnetic field is more than 30 times that of the incident waves, showing a strong diamagnetic effect. The magnetic fields oscillate and the current loop varies from clockwise to counterclockwise and vice versa. Fig. 4 shows the relative surface charge density distribution on the left and right surfaces of the trench at $t=0$ calculated by

$$\rho_e=\varepsilon_0\mathbf{n}\bullet(\mathbf{E}_1-\mathbf{E}_2) \tag{2}$$

where ε_0 is the electric permittivity of vacuum; $\mathbf{E}_1$ and $\mathbf{E}_2$ are the electric fields on either side of the surface, and $\mathbf{n}$ is a unit normal vector to the surface from side 1 to side 2. The change density is normalized by ρ_c which is the charge density at the center of the surface ($z=100$ nm). The sign and magnitude of the charge density also change with time. Corresponding to the electric field in Fig. 3(a), when

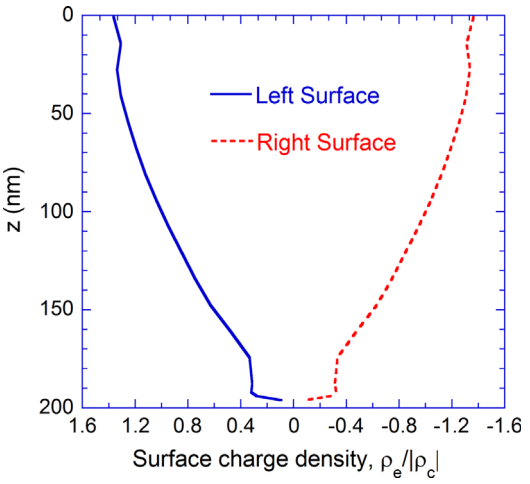

Fig. 4. Relative charge density distribution along the side walls of the trench for the grating with the same parameters as in Fig. 3. Note that $z=0$ is the opening and $z=200$ nm is the bottom of the grooves.

the resonance happens, charges tend to accumulate at the upper corner of the grating and this in turn creates a strong electric field.

Based on the closed current loop, an equivalent LC circuit model [9,26,27,29] shown in Fig. 1 is used to predict the magnetic resonance condition. The air in the trenches serves as a dielectric capacitor and the surrounding metallic material is treated as a conductor. Excluding the effect of resistance, conductor elements have inductance effects resulting from charge acceleration under a time-varying external electric field. Thus, the current necessarily has a phase delay with respect to the electric field [32]. The kinetic inductance L_k is introduced to model the frequency-dependent complex impedance of the metal, $Z_k \equiv R_k - i\omega L_k$, where ω is the angular frequency. The impedance can also be expressed as

$$Z_k = \frac{s}{\sigma A_{eff}} \tag{3}$$

where s is the total length of current path in the metal and A_{eff} is the effective cross-section area of the induced electric current. For the deep grating structure, $s=2h+b$ and $A_{eff}=\delta l$, where $\delta=\lambda/2\pi\kappa$ is the penetration depth of electric field, in which κ is the extinction coefficient, and l is the length in the y direction that can be set to unity for 1D gratings. Note that the penetration depth of electric field is twice as much as that of the radiative power, which was used in previous LC models [26,27]. However, the field penetration depth appears to be a better approximation since only the current flow is dealt with. After some manipulations, it can be shown that

$$L_k = -\frac{2h+b}{\varepsilon_0\omega^2 l\delta}\frac{\varepsilon'}{(\varepsilon'^2+\varepsilon''^2)} \tag{4}$$

where ε' and ε'' are the real and imaginary parts of the dielectric function ε, respectively. Since walls on both sides of the groove are close to each other, mutual inductance L_m also needs to be included and can be evaluated from the parallel-plate inductance formula:

$$L_m = \mu_0\frac{hb}{l} \tag{5}$$

where μ_0 is the permeability of vacuum. The capacitance of the air inside the trench can be approximated by

$$C = c'\varepsilon_0\frac{hl}{b} \tag{6}$$

where c' is a numerical factor between 0 and 1 accounting for the nonuniform charge distribution between the ridges of the grating [27,28]. If the charges are uniformly distributed on the surfaces around the trench, c' would be 1 and Eq. (6) would degenerate to the capacitance between two infinitely long parallel plates. The actual charge distribution is complicated as shown in Fig. 4 and the non-uniform charge density distribution suggests the existence of fringe effect [33]. If the charge were linearly distributed along the surfaces on both sides of the grooves and the charge density increases from zero at the bottom to a maximum at the opening of the grating, then c' would be 0.5. Without using a full-wave model, c' can be taken as an adjustable parameter that is about 0.5. By using an effective parameter c', one could still evaluate the capacitance of the cavity by a simple formula and thus make it possible to capture the fundamental physics with a simple model. The total impedance of the LC circuit can therefore be expressed by

$$Z_{tot} = i\omega\left(L_k + L_m - \frac{1}{\omega^2 C}\right) \tag{7}$$

The resistance elements are neglected for simplicity, since they do not affect the resonance frequency. By setting $Z_{tot}=0$, one obtains the magnetic resonance wavelength as

$$\lambda_R = 2\pi c_0\sqrt{(L_k+L_m)C} \tag{8}$$

which is an implicit equation because L_k is frequency- or wavelength-dependent. Note that l does not show up in this equation and can be assumed unity in later discussions. This may also explain why the resonance wavelength predicted for a 1D grating is similar for a 2D grating with the same geometry in the x–z plane. Since the thickness of the plates is much greater than δ, each groove can be considered as an isolated unit. As an example, if $c'=0.5$ is used in Eq. (6), the LC model yields a resonance at $\lambda_R=2.78$ μm, which agrees well with the RCWA simulation. The feasibility of using the LC-circuit model to explain the parameter dependence of the resonance wavelength in deep gratings with different materials is discussed next.

3. Results and discussion

3.1. Trench width dependence of the MP resonance

The emittance contour shown in Fig. 5(a) demonstrates the effect of the trench width on the resonance frequency of the Ag grating with $\Lambda=400$ nm and $h=200$ nm. The major bright band is attributed to the fundamental MP mode that is the focus of the present study and the other bands are higher-order MP modes. At sufficiently large trench width, the dispersion curve tends to become flat (not shown in the figure), but bents toward lower wavenumbers when the trench width decreases, suggesting a significant dependence of the resonance frequency on the trench width in deep gratings. The green diamond marks indicate those predicted

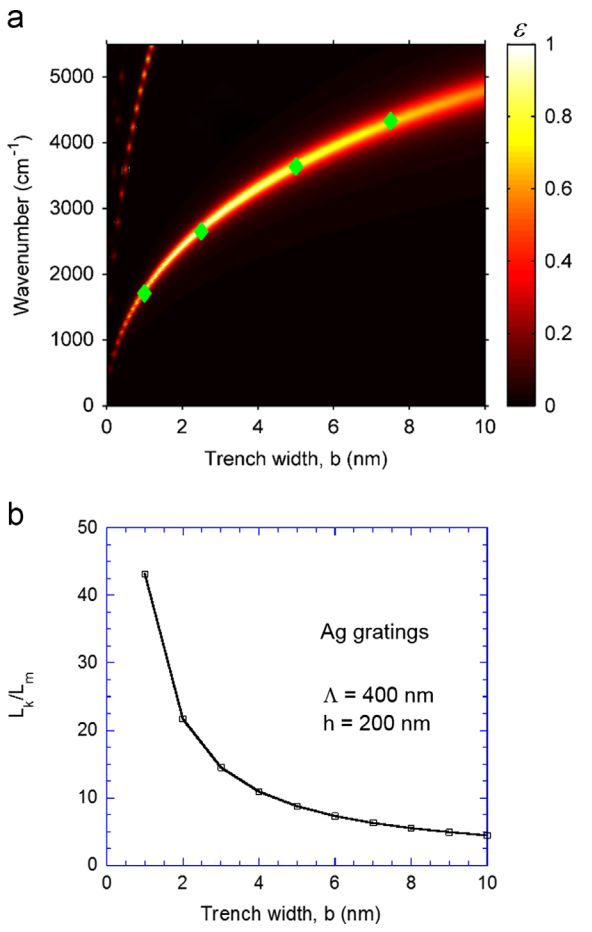

Fig. 5. (a) Emittance contour of Ag gratings with $\Lambda = 400$ nm and $h = 200$ nm calculated by RCWA, where the diamond marks indicate the resonance conditions predicted by the LC model and (b) ratio of the kinetic inductance to the magnetic inductance (L_k/L_m) calculated at the MP resonance.

from the LC model in this and the rest contour plots. It can be seen that the LC model agrees very well with the dispersion curve determined from the full-wave RCWA calculation. When the trench width is narrow, the resonance wavelength increases significantly with decreasing trench width, resulting in a cutoff wavelength that can be more than 10 times the grating height. This effect is further explained by comparing the magnitude of the inductances in the LC model as discussed in the following.

According to Eqs. (4) and (5), for a 1D deep grating with fixed period and height, L_m depends linearly on the trench width b but is independent of the frequency. However, L_k depends little on b due to the fact that $2h \gg b$, but depends strongly on the frequency or wavelength. On the other hand, the capacitance is inversely proportional to b based on Eq. (6). According to Eq. (8), if L_k is negligible compared with L_m, the resonance wavelength depends on the product of L_mC, which is independent of b. The ratio L_k/L_m at the MP resonance is plotted in Fig. 5(b) as a function of b under the condition showing in Fig. 5(a). In this case, L_k is much greater than L_m. A large kinetic inductance shifts the resonance to longer wavelengths according to Eq. (8). As the trench width increases, L_m increases and the ratio L_k/L_m becomes smaller and subsequently the resonance frequency increases and eventually reaches a constant that

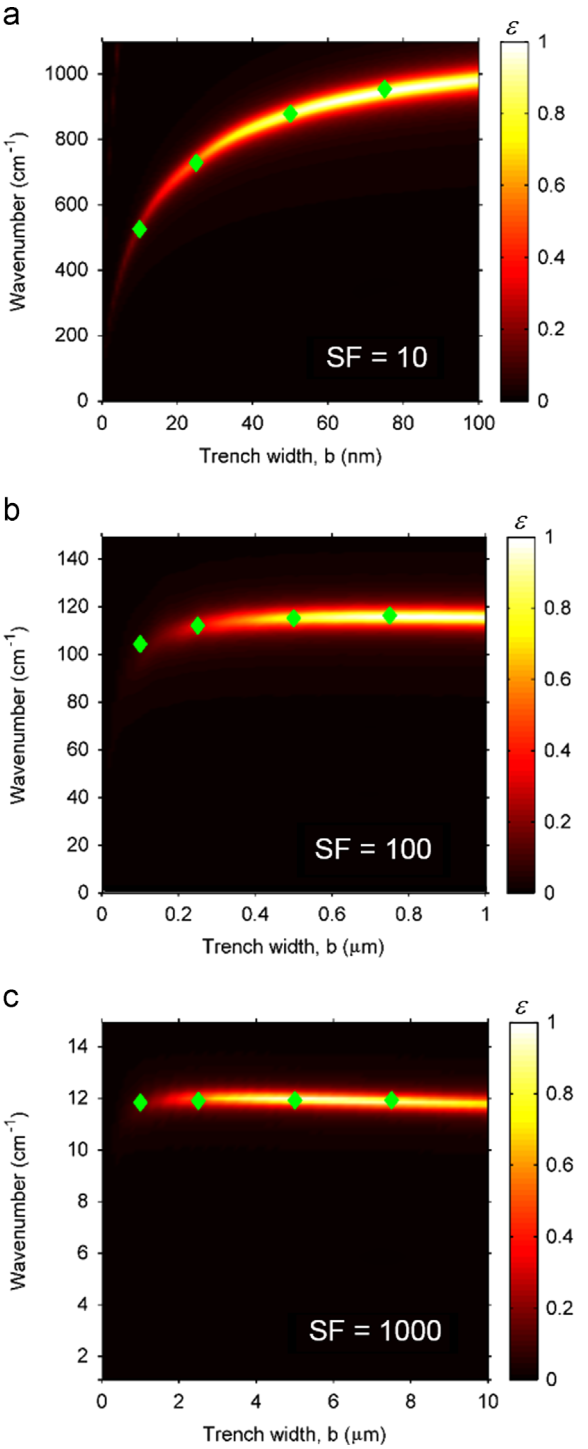

Fig. 6. Emittance contours and LC model predictions (shown as diamonds) of Ag gratings when the geometric dimensions are scaled up compared with the based case in Fig. 2(a): (a) $SF = 10$; (b) $SF = 100$; and (c) $SF = 1000$.

is independent of b. Of course, magnetic resonance can occur at different spectral regions with different geometric scales. The scalability of MP resonance is discussed in subsequent section.

3.2. Scalability of the MP resonance

The effects of the kinetic inductance on the resonance wavelength can be better understood if we consider similar MP resonances in different frequency ranges. Fig. 6 shows MPs in three deep gratings with the same aspect ratio but the dimensions are increased by a scaling factor (SF) of 10, 100, and 1000 compared with those for Fig. 5. The different shapes of the dispersion curves are due to the different frequency dependence of the dielectric function of Ag. For metals in the long-wavelength region, $\varepsilon' \ll \varepsilon''$, resulting in a decrease of L_k/L_m as the dimensions (and wavelength) are scaled up. With large SF values, resonances are very weak and cannot exist toward the left end of the emittance contour. As shown in Fig. 6(b) and (c), the resonance frequency is essentially independent of the trench width. In the low frequency limit, L_k is negligible and Eq. (8) yields an asymptotic value for the resonance wavelength:

$$\lambda_A = 2\pi c_0 \sqrt{L_m C} = 2\pi h \sqrt{c'} \tag{9}$$

which gives $\lambda_A \approx 4.4$ h for $c' = 0.5$ and is close to that predicted from the cavity mode.

The values of the physical properties corresponding to the resonances are listed in Table 1 for the MP mode in Fig. 2(a) as well as three scaled up geometries. The value of c' listed in Table 1 is treated as an adjustable parameter to match with the MP resonance peaks for each scaling factor, but is assumed to be independent of the trench width. It can be seen that c' is very close to 0.5 and the LC model agrees with the RCWA calculation well as demonstrated in Figs. 5(a) and 6. The last column of Table 1 shows the Q-factor, which is the ratio of the resonance frequency over the full width at half maximum of the emittance peak for MP resonance. A large Q-factor indicates a relative sharp peak or more coherent thermal emission. It can be seen that the Q-factor increases with the scaling factor or resonance wavelength. The reason needs further exploration.

3.3. MP resonance in doped silicon and tungsten thermal emitters

Since for the aforementioned deep gratings with the aspect ratio more than 20, even though the Bosch process [34] and nanoimprint lithography [35] could be used, the fabrication of the structure is still very challenging. For a practical structure for thermal emission control, structures with a somewhat larger trench width is certainly designed if high emittance can still be achieved. For Ag gratings as shown in Fig. 7 for $\Lambda = 4$ μm and $h = 2$ μm, when $b > 0.5$ μm, the resonance becomes very weak. For example, for $b = 0.8$ μm, the peak emittance is only 0.07, which is too small for use as a thermal emitter. Note that Ag has a very high extinction coefficient and the electromagnetic field can only penetrate inside by a very short distance. Strong field coupling between the two sides of the trench happens only when the trench is very narrow. Additionally, since the relative penetration depth (δ/λ) decreases as λ increases, it is even more difficult for the field to couple and create MP resonance at longer wavelengths.

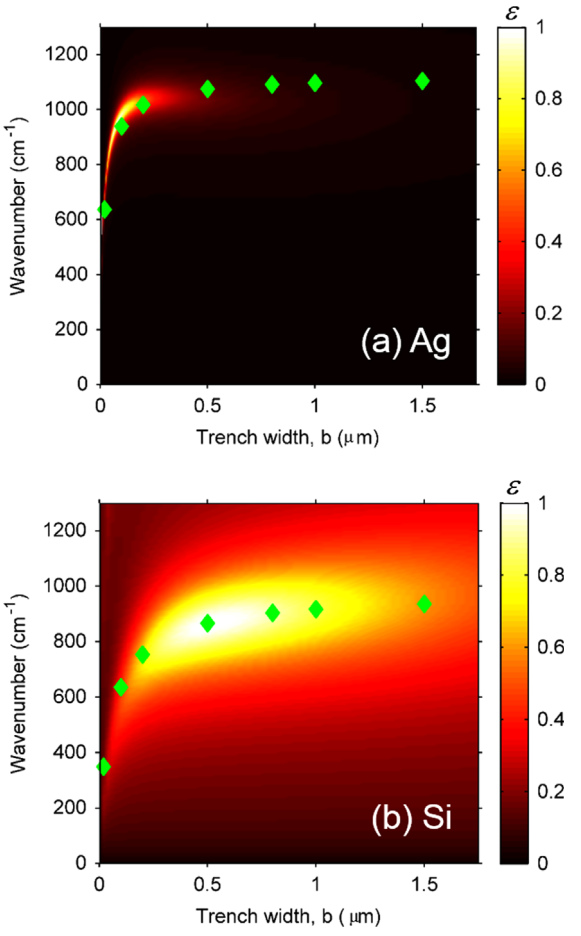

Fig. 7. Emittance contours with LC model predictions marked as diamonds of (a) Ag gratings with $\Lambda = 4$ μm and $h = 2$ μm; (b) doped Si gratings with the same period and height.

Table 1
Physical properties for MP resonances in Ag gratings with different scaling factors. The base case for $SF = 1$ is the same as for Fig. 2(a).

SF	Wavenumber (cm^{-1})	Wavelength (μm)	L_k (Wb/A)	L_m (Wb/A)	C (C/V)	c'	Q-factor
1	3650	2.74	1.10×10^{-20}	1.26×10^{-21}	1.72×10^{-10}	0.49	14.9
10	877.4	11.4	1.09×10^{-19}	1.26×10^{-19}	1.56×10^{-10}	0.44	16.3
100	115.2	86.8	7.83×10^{-19}	1.26×10^{-17}	1.59×10^{-10}	0.45	19.2
1000	11.92	838.9	4.65×10^{-18}	1.26×10^{-15}	1.57×10^{-10}	0.44	25.4

The aforementioned problem can be alleviated by using heavily-doped Si because of its smaller plasma frequency and relatively small extinction coefficient as compared to Ag. Since the field can penetrate deeper into doped Si, it may be easier for the two surfaces in the trench to couple at a relatively large distance. The dielectric function for p-type doped Si is taken from [36], assuming the temperature is at 300 K with a doping concentration 10^{21} cm^{-3}. Fig. 7(b) shows the emittance contour for doped Si with the same geometries as for Fig. 7(a). The resonance is much stronger and broader for $0.25\ \mu m < b < 1\ \mu m$ with doped Si than with Ag. The broadening effect is due to the large scattering rate or resistance of doped Si compared to Ag. The MP resonance becomes weaker if b is increased to beyond 1 μm.

Fig. 8 shows the emittance spectra for doped Si gratings with different scaling factors so that the MPs are excited in different wavelength ranges. The grating with parameters $\Lambda=400$ nm, $h=200$ nm, and $b=80$ nm is not included, because doped-Si does not exhibit metallic behavior in the near-infrared. The physical properties at the MP modes are listed in Table 2. Due to the effect of the kinetic inductance, the resonance wavelength is shifted to 5.6 times the grating height in Fig. 8(a) and the ratio drops to 4.7 in Fig. 8(d). Note that the resonance wavelength in Fig. 8(d) is about 1 cm, indicating the scalability of MPs up to the microwave region. One could also argue that the MP model merely predicts the cavity modes when the kinetic inductance is negligible. It appears that the kinetic inductance is the key for the coupled SPPs between the two sides of the grooves. Furthermore, one could use the waveguide mode to explain the guided wave nature for deep gratings. All the explanations appear to be consistent but are from different aspects. The advantage of using the LC model is due to its simplicity and ability to explain the resonance behavior with scalability and for different materials. Relatively lower Q-factors listed in Table 2 indicate the broadening effect of doped Si due to its high electrical resistance, showing a difference of MP resonances with doped Si gratings with those in Ag deep gratings.

The adjustable c' values listed in Table 2 are very close for the four cases. The value 0.64 is also used for the LC model prediction in Fig. 7(b), which agrees well with the full-wave

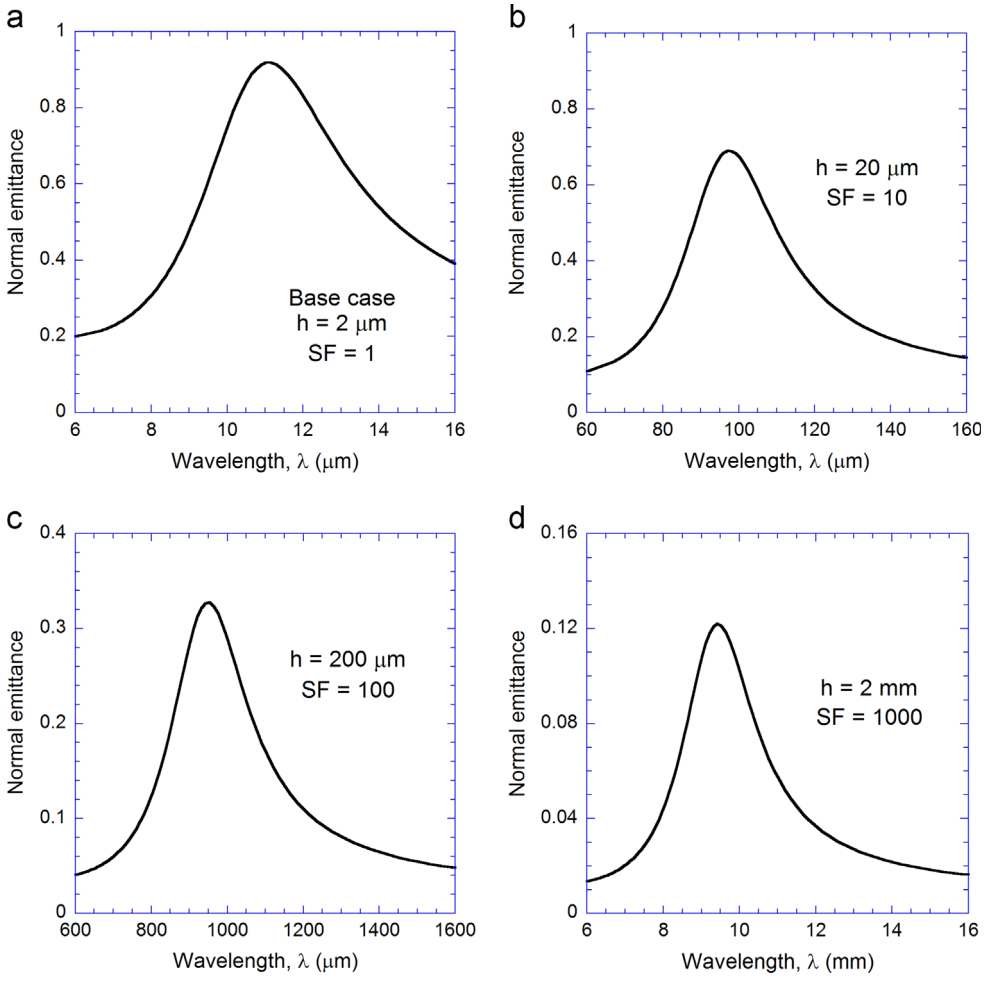

Fig. 8. Emittance spectra for doped Si deep gratings with the base geometry ($SF=1$) of $\Lambda=4$ μm, $h=2$ μm, and $b=0.8$ μm and for different scaling factors: (a) $SF=1$; (b) $SF=10$; (c) $SF=100$; and (d) $SF=1000$.

Table 2
Physical properties for MP resonances in doped Si gratings with different scaling factors. The base case corresponding to $\Lambda=4$ μm, $h=2$ μm, and $b=0.8$ μm.

SF	Wavenumber (cm^{-1})	Wavelength (μm)	L_k (Wb/A)	L_m (Wb/A)	C (C/V)	c'	*Q*-factor
1	908	11.1	4.27×10^{-19}	2.01×10^{-18}	1.42×10^{-11}	0.64	2.0
10	103	97.2	1.34×10^{-18}	2.01×10^{-16}	1.32×10^{-11}	0.59	2.9
100	10.5	952	4.12×10^{-18}	2.01×10^{-14}	1.27×10^{-11}	0.57	3.5
1000	1.06	9420	1.30×10^{-17}	2.01×10^{-12}	1.24×10^{-11}	0.56	3.8

simulation. It should be mentioned that $c'=0.5$ is used in the predictions in Fig. 7(a). Since trench width covers a wide range, the LC model predictions with a fixed c' value may deviate somewhat from the full-wave simulation when b is greater than 1 μm [37]. Also, the value of c' is related to the choice of the penetration depth used in Eq. (4) to evaluate the kinetic inductance. Even the field penetration depth work well in previous discussions, the penetration depth is only an approximation and, for some lossy materials, the power penetration depth might be more reasonable. Take the 2D tungsten grating thermal emitter in [8] as an example, the normal emittance spectrum is very similar for the 1D grating with the same geometric parameters in the x direction and extended to infinite in the y direction, as shown in Fig. 9. The optical properties of tungsten are obtained from [38] and linear interpolation is used between adjacent data points. The advantage of using a 2D nanostructure over 1D nanostructure is that it allows high emittance, particularly near 1.5 μm, for both polarizations [25]. The emittance peak at $\lambda=1.55$ μm is direction independent for TM waves and the resonance wavelength is 7.6 times of the grating height. From the charge density and field distribution (not shown here), it can be convinced that MP resonance is responsible for this peak. Furthermore, one can use $c'=0.58$ to well predict this MP resonance wavelength by using the power penetration depth (which is half of the electric field penetration depth) to evaluate the kinetic inductance. In addition, if one uses the power penetration depth to evaluate the kinetic inductance for doped Si gratings, the c' listed in Table 2 for $SF=1$ would be 0.55 and closer to 0.5. On the other hand, the c' values for other cases listed in Table 2 change little since L_k/L_m is very small.

Deep cavity gratings can also be used to create high broadband emittance. Unlike the coupling between non-periodic grating and waveguide mode [39] or some other symmetric-braking structures [40], MPs are highly localized and insensitive to the grating period. However, since MPs are sensitive to the height and width of the cavity, one may achieve broadband emittance by distribute cavities with different geometries within one period that can excite MPs at different frequencies. Similar structures have been investigated by researchers previously [3,7,41]. For those structures, the effective medium theory cannot be applied to calculate the emittance due to the complex geometric structures and full-wave simulation would be required.

One should note that the MP resonance does not exist for TE waves in 1D deep gratings. Even though the cavity mode explained by Eq. (1) is supposed to work for both TE and TM waves [24], the resonances associated with the height dimension do not show up for TE waves. This is because tangential component of electric field has to be continuous

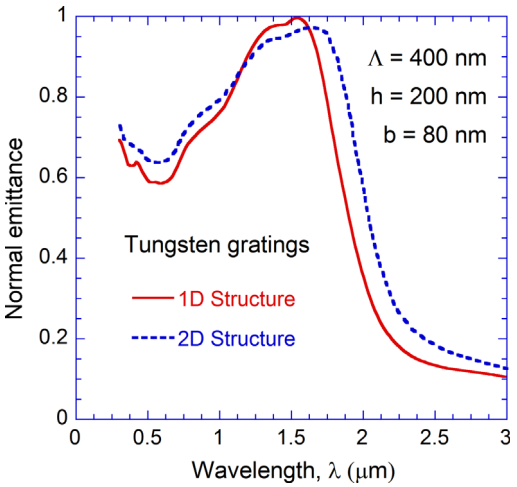

Fig. 9. Emittance spectra for 1D and 2D tungsten gratings with $\Lambda=400$ nm, $h=200$ nm, and $b=80$ nm. The 2D grating has the same geometries in both x and y directions.

across the boundary of the trench, at least the first order resonance associated with the later dimension of the trench should exist (that is, l cannot be zero) for TE waves. Take the case in Fig. 7(a) with $b=0.8$ μm as an example, the normal emittance of spectrum for TE waves only show a cutoff wavelength around 1.6 μm, which is due to the resonance in the x direction associated with the trench width [24]. Similar results were obtained for slit array gratings [42], where the cavity modes or trapped modes can enhance the transmittance [43–45].

4. Conclusions

This study demonstrates that MPs can provide a convincing explanation of the fundamental resonance in deep gratings. By employing a simple LC model, the resonance wavelength can be quantitatively predicted. Due to the effect of the kinetic inductance, the cutoff wavelength can be extended to more than ten times the grating height for very narrow grooves. The cutoff wavelength predicted by the conventional cavity resonance model agrees with the prediction of MPs only when the kinetic inductance is negligibly small compared with the mutual inductance. Ag and doped Si are considered and the resonance frequency can be scaled from near-infrared to microwave region by scaling the grating geometries. The MP model can also explain the thermal emission peak in 2D tungsten grating emitters. Caution should be taken when choosing the penetration depth and the constant c' for high-loss

materials. This study further clarifies one of the underlying mechanisms of optical resonance in deep gratings, which can benefit the future design of thermal emitters based on 1D and 2D grating structures.

Acknowledgement

This work is supported by the US Department of Energy (DE-FG02-06ER46343). The authors would like to thank Dr. Liping Wang, Dr. Atsushi Sakurai, Mr. Jesse Watjen, and Mr. Xianglei Liu for valuable comments and discussions.

References

[1] Pillai S, Catchpole KR, Trupke T, Green MA. Surface plasmon enhanced silicon solar cells. J Appl Phys 2007;101:093105–8.
[2] Sergeant NP, Agrawal M, Peumans P. High performance solar-selective absorbers using coated sub-wavelength gratings. Opt Express 2010;18:5525–40.
[3] Yang L, Xuan Y, Han Y, Tan J. Investigation on the performance enhancement of silicon solar cells with an assembly grating structure. Energy Convers Manage 2012;54:30–7.
[4] Hajimirza S, El Hitti G, Heltzel A, Howell J. Specification of micro-nanoscale radiative patterns using inverse analysis for increasing solar panel efficiency. J Heat Transf 2012;134:102702.
[5] Basu S, Chen Y-B, Zhang ZM. Microscale radiation in thermophotovoltaic devices – a review. Int J Energy Res 2007;31:689–716.
[6] Sai H, Yugami H. Thermophotovoltaic generation with selective radiators based on tungsten surface gratings. Appl Phys Lett 2004;85:3399–401.
[7] Chen Y-B, Zhang ZM. Design of tungsten complex gratings for thermophotovoltaic radiators. Opt Commun 2007;269:411–7.
[8] Chen Y-B, Tan KH. The profile optimization of periodic nanostructures for wavelength-selective thermophotovoltaic emitters. Int J Heat Mass Transf 2010;53:5542–51.
[9] Wang LP, Zhang ZM. Wavelength-selective and diffuse emitter enhanced by magnetic polaritons for thermophotovoltaics. Appl Phys Lett 2012;100:063902.
[10] Zhang ZM, Wang LP. Measurements and modeling of the spectral and directional radiative properties of micro/nanostructured materials. Int J Thermophys 2013;34:2209–42.
[11] Hesketh PJ, Zemel JN, Gebhart B. Organ pipe radiant modes of periodic micromachined silicon surfaces. Nature 1986;324:549–51.
[12] Hesketh PJ, Zemel JN, Gebhart B. Polarized spectral emittance from periodic micromachined surfaces. I. Doped silicon: the normal direction. Phys Rev B 1988;37:10795–802.
[13] Maruyama S, Kashiwa T, Yugami H, Esashi M. Thermal radiation from two-dimensionally confined modes in microcavities. Appl Phys Lett 2001;79:1393–5.
[14] Kusunoki F, Kohama T, Hiroshima T, Fukumoto S, Takahara J, Kobayashi T. Narrow-band thermal radiation with low directivity by resonant modes inside tungsten microcavities. Jpn J Appl Phys 2004;43:5253–8.
[15] Huang J, Xuan Y, Li Q. Narrow-band spectral features of structured silver surface with rectangular resonant cavities. J Quant Spectrosc Radiat Transf 2011;112:839–46.
[16] Mattiucci N, D'Aguanno G, Alu A, Argyropoulos C, Foreman JV, Bloemer MJ. Taming the thermal emissivity of metals: a metamaterial approach. Appl Phys Lett 2012;100:201109.
[17] Gordon R, Brolo A. Increased cut-off wavelength for a subwavelength hole in a real metal. Opt Express 2005;13:1933–8.
[18] Suckling JR, Hibbins AP, Lockyear MJ, Preist TW, Sambles JR, Lawrence CR. Finite conductance governs the resonance transmission of thin metal slits at microwave frequencies. Phys Rev Lett 2004;92:147401.
[19] Dahan N, Niv A, Biener G, Gorodetski Y, Kleiner V, Hasman E. Enhanced coherency of thermal emission: beyond the limitation imposed by delocalized surface waves. Phys Rev B 2007;76:045427.
[20] Sobnack MB, Tan WC, Wanstall NP, Preist TW, Sambles JR. Stationary surface plasmons on a zero-order metal grating. Phys Rev Lett 1998;80:5667–70.
[21] Wanstall NP, Preist TW, Tan WC, Sobnack MB, Sambles JR. Standing-wave surface-plasmon resonances with overhanging zero-order metal gratings. J Opt Soc Am A 1998;15:2869–76.
[22] Xuan Y, Zhang Y. Investigation on the physical mechanism of magnetic plasmons polaritons. J Quant Spectrosc Radiat Transf 2014;132:43–51.
[23] Pardo F, Bouchon P, Haïdar R, Pelouard J-L. Light funneling mechanism explained by magnetoelectric interference. Phys Rev Lett 2011;107:093902.
[24] Nguyen-Huu N, Chen Y-B, Lo Y-L. Development of a polarization-insensitive thermophotovoltaic emitter with a binary grating. Opt Express 2012;20:5882–90.
[25] Zhao B, Wang L, Shuai Y, Zhang ZM. Thermophotovoltaic emitters based on a two-dimensional grating/thin-film nanostructure. Int J Heat Mass Transf 2013;67:637–45.
[26] Wang LP, Zhang ZM. Resonance transmission or absorption in deep gratings explained by magnetic polaritons. Appl Phys Lett 2009;95:111904.
[27] Wang LP, Zhang ZM. Phonon-mediated magnetic polaritons in the infrared region. Opt Express 2011;19:A126–35.
[28] Zhou J, Economon EN, Koschny T, Soukoulis CM. Unifying approach to left-handed material design. Opt Lett 2006;31:3620–2.
[29] Engheta N. Circuits with light at nanoscales: optical nanocircuits inspired by metamaterials. Science 2007;317:1698–702.
[30] Zhang ZM. Nano/microscale heat transfer. New York: McGraw-Hill; 2007.
[31] Modest MF. Radiative heat transfer. 2nd ed.San Diego: Academic Press; 2003.
[32] Solymar L, Shamonina E. Waves in metamaterials.Oxford: Oxford University Press; 2009.
[33] Nishiyama H, Nakamura M. Form and capacitance of parallel-plate capacitors. IEEE Trans Compon Packag Manuf Technol Pt A 1994;17:477–84.
[34] Rinnerbauer V, Ndao S, Yeng YX, Senkevich JJ, Jensen KF, Joannopoulos JD, et al. Large-area fabrication of high aspect ratio tantalum photonic crystals for high-temperature selective emitters. J Vac Sci Technol B 2013;31:011802–7.
[35] Guo LJ. Nanoimprint lithography: methods and material requirements. Adv Mater 2007;19:495–513.
[36] Basu S, Lee BJ, Zhang ZM. Infrared radiative properties of heavily doped silicon at room temperature. J Heat Transf 2010;132:023301.
[37] Chen C-J, Chen J-S, Chen Y-B. Optical responses from lossy metallic slit arrays under the excitation of a magnetic polariton. J Opt Soc Am B 2011;28:1798–806.
[38] Palik ED. Handbook of optical constants of solids.San Diego, CA: Academic Press; 1985.
[39] Pala RA, Liu JSQ, Barnard ES, Askarov D, Garnett EC, Fan S, et al. Optimization of non-periodic plasmonic light-trapping layers for thin-film solar cells. Nat Commun 2013;4:2095.
[40] Tok RU, Şendur K. Engineering the broadband spectrum of close-packed plasmonic honeycomb array surfaces. J Quant Spectrosc Radiat Transf 2013;120:70–80.
[41] Cheng Q, Li P, Lu J, Yu X, Zhou H. Silicon complex grating with different groove depths as an absorber for solar cells. J Quant Spectrosc Radiat Transf 2014;132:70–9.
[42] Lee BJ, Chen YB, Zhang ZM. Transmission enhancement through nanoscale metallic slit arrays from the visible to mid-infrared. J Comput Theor Nanosci 2008;5:201–13.
[43] Borisov AG, García de Abajo FJ, Shabanov SV. Role of electromagnetic trapped modes in extraordinary transmission in nanostructured materials. Phys Rev B 2005;71:075408.
[44] Lu Y, Cho MH, Lee Y, Rhee JY. Polarization-independent extraordinary optical transmission in one-dimensional metallic gratings with broad slits. Appl Phys Lett 2008;93:061102.
[45] Selcuk S, Woo K, Tanner DB, Hebard AF, Borisov AG, Shabanov SV. Trapped electromagnetic modes and scaling in the transmittance of perforated metal films. Phys Rev Lett 2006;97:067403.